Amplitude expansion of the binary phase-field-crystal model

K. R. Elder
Department of Physics, Oakland University, Rochester, Michigan 48309, USA

Zhi-Feng Huang
Department of Physics and Astronomy, Wayne State University, Detroit, Michigan 48201, USA

Nikolas Provatas
Department of Materials Science and Engineering and Brockhouse Institute for Materials Research, McMaster University, Hamilton, Ontario, Canada L8S-4L7

(Received 4 October 2009; published 7 January 2010)

Amplitude representations of a binary phase-field-crystal model are developed for a two-dimensional triangular lattice and three-dimensional bcc and fcc crystal structures. The relationship between these amplitude equations and the standard phase-field models for binary-alloy solidification with elasticity are derived, providing an explicit connection between phase-field-crystal and phase-field models. Sample simulations of solute migration at grain boundaries, eutectic solidification, and quantum dot formation on nanomembranes are also presented.

DOI: 10.1103/PhysRevE.81.011602 PACS number(s): 81.10.Aj, 81.15.Aa, 81.30.−t, 61.72.Bb

I. INTRODUCTION

The development and analysis of continuum field theories to model complex nonequilibrium structures or spatial patterns have made a tremendous impact in many areas of research in condensed-matter and materials physics. A central idea in the development of such models is the recognition that the patterns are controlled by the *type* and *interaction* of *defects* that define the patterns. For example, in spinodal decomposition, *surfaces* between different atomic species can interact through *diffusion* in the bulk providing one of the mechanisms for the phase segregation process. In block copolymer systems [1], *disclinations* interact through *elastic fields* and control the ordering of lamellar phases. While it is desirable that models of these processes be derived from some fundamental atomic theory, they are frequently phenomenologically proposed. Classic phenomenological models include the Ginzburg-Landau theory of superconductivity [2] and the Cahn-Hilliard-Cook theory of phase segregation [3,4].

Several years ago, a phase-field model of crystallization was phenomenologically proposed by exploiting the properties of free-energy functionals that are minimized by periodic fields. In crystallization, this field is interpreted as the atomic number density (ρ), which is uniform in a liquid phase and is typically periodic in the solid phase. By incorporating elasticity, dislocations, and multiple crystal orientations, such functionals naturally incorporate the type and interaction of the defects that control many crystallization phenomena. This so-called phase-field-crystal (PFC) model [5,6] has been used to study glass formation [7], climb and glide dynamics [8], premelting at grain boundaries [9,10], epitaxial growth [11,12], commensurate to incommensurate transitions [13,14], sliding friction phenomena [15], and the yield strength of polycrystals [5,6,16,17]. More recently, a simple binary phase-field-crystal model was developed [18] that couples the features of the PFC model of a pure material with a concentration field so that eutectic growth, spinodal decomposition, and dendritic growth can also be studied. As shown in Refs. [7,18], PFC models can be linked with classical density-functional theory (CDFT) and dynamical density-functional theory [7,19,20] although the approximations are quite drastic. For example, in recent studies on Fe [21] and colloidal systems [20], CDFT predicts that ρ is very sharply peaked in space (at atomic lattice positions) while the PFC solutions are almost sinusoidal in space. Nevertheless, these same studies seem to indicate that the parameters entering PFC models can be adjusted to match experimental quantities.

While the periodic structure of PFC models is essential for describing elasticity and plasticity, it is very inconvenient for numerical calculations. For example, PFC simulations typically require 8^d (where d is dimension) spatial grid points per atomic lattice site. Obviously, this limits the method to relatively small systems, although several new computational algorithms have been developed that can significantly extend the applicability of both pure [22–25] and binary PFC models [26]. To alleviate this limitation, an amplitude expansion of the PFC model was developed by Goldenfeld *et al.* [27–29]. To understand the idea behind such expansions, it is useful to consider a one-dimensional equilibrium state of the form $n=A\sin(qx)$, where the amplitude, A, is zero in the liquid and finite in the solid state. While the field n varies rapidly in space, on a length scale set by $\lambda=2\pi/q$, the amplitude A is uniform in crystalline regions and only varies near dislocations and liquid solid surfaces. Deformations of the crystal lattice can be represented by spatial variations in the phase of the amplitude. Using this amplitude representation, Athreya *et al.* [30] were able to apply adaptive mesh refinement to simulate grain growth on micron scales while simultaneously resolving atomic scale structures at interfaces. This remarkable achievement suggests that the development of amplitude expansions is very promising for computational materials research. More recently, this expansion has been extended to include spatial variations in the average number density in two and three dimensions [31].

In addition to greatly increasing computational efficiency, amplitude representations of PFC models can also be exploited to establish a link between PFC-type models and traditional phase-field models. This link provides insight into the specific terms that enter the bulk free-energy and gradient-energy coefficients of traditional phase-field models [32–35]. Since the relationships between the parameters that enter phase-field models and sharp interface models are well established [36–38], the relationship between parameters in PFC models to sharp interface models can then be established.

In this paper, amplitude expansions are developed for triangular (two-dimensional, 2D), bcc, and fcc crystal symmetries. The method of multiple scales expansion methods employed by Yeon *et al.* [31] is used. In the small deformation limit, the expansions are shown to reproduce standard phase-field models of solidification and eutectic growth which incorporate elasticity and solute segregation effects. Sample simulations of grain-boundary segregation, eutectic solidification, and quantum dot growth on nanomembranes are also presented to illustrate the flexibility of the amplitude equations.

II. BINARY PHASE FIELD CRYSTAL MODEL

As discussed above, the binary-alloy PFC model developed recently [18] can incorporate the important features of solidification, phase segregation, and solute expansion in alloy systems, in addition to the elasticity, plasticity, and multiple crystal orientations that characterize the crystalline state. For an alloy consisting of A and B atoms, the model can be written in the case of equal atomic mobilities of the constituents as

$$\frac{\partial n}{\partial \tau} = M\nabla^2 \frac{\delta \mathcal{F}}{\delta n},$$

$$\frac{\partial \psi}{\partial \tau} = M\nabla^2 \frac{\delta \mathcal{F}}{\delta \psi}, \tag{1}$$

where M is the mobility and τ is time. In principle, random thermal fluctuations can be included in these equations but are left of for simplicity. The field n is the dimensionless number density difference given by $n \equiv (\rho_A + \rho_B - \rho_\ell)/\rho_\ell$, where ρ_A, ρ_B, and ρ_ℓ are the atomic number densities of A atoms, B atoms, and a reference liquid, respectively. The field $\psi = (\rho_A - \rho_B)/\rho_\ell$ plays the role of a concentration field. The free energy is given by

$$\frac{\Delta \mathcal{F}}{k_B T \rho_l} = \int d\vec{r} \left[\frac{B^\ell}{2} n^2 + B^x \frac{n}{2} \Lambda n - \frac{t}{3} n^3 + \frac{v}{4} n^4 + \gamma \psi + \omega \frac{\psi^2}{2} + u \frac{\psi^4}{4} + \frac{K'}{2} |\vec{\nabla} \psi|^2 \right], \tag{2}$$

where $\Lambda \equiv 2R^2\nabla^2 + R^4\nabla^4$ and t, v, γ, ω, u and K' are constants. This model is essentially a very approximate version of the classical density-functional theory (CDFT) of freezing proposed by Ramakrishnan and Yussouff [39] in which the Helmholtz free-energy functional is expanded in a functional

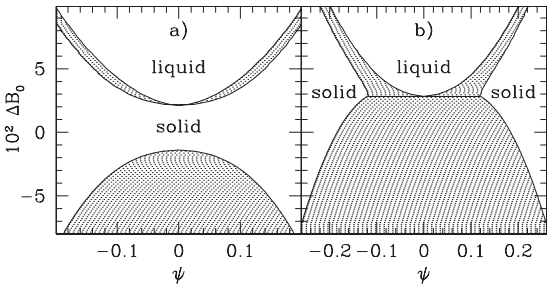

FIG. 1. Sample phase diagram for two-dimensional triangular system with parameter set $(B_0^x, B_2^\ell, v, t, \alpha, u) = (1, -1.8, 1, 3/5, 0.30, 4)$. Also $\omega = 0.088$ and 0.008 in (a) and (b), respectively. In each panel, the filled regions correspond to regions of phase coexistence.

Taylor series of the number density field. Equation (2) is obtained by truncating the functional Taylor-series expansion for a binary system at second order as proposed by Rick and Haymet [40], expanding to order n^4 and ψ^4 and by fitting the first peak in the second-order direct correlation function in Fourier space [18]. While the resulting free-energy functional is a crude approximation to the second-order model proposed by Rick and Haymet [40] or the more sophisticated weighted DFT binary model proposed by Denton and Ashcroft [41], it does provide a computational efficient model that incorporates elasticity, plasticity, multicrystal orientations, solidification, and phase segregation. In addition, as will be shown, it reduces to standard continuum models of elasticity, solidification, and phase segregation in the appropriate limit. The parameters B^ℓ, B^x, and R depend on ψ and in the simplest nontrivial case can be set to $B^\ell \equiv B_0^\ell + B_2^\ell \psi^2$, $B^x = B_0^x$, and $R = R_0(1 + \alpha\psi)$. In this context, the "simplest nontrivial case" refers to a parameterization that leads to typical phase diagram containing liquid-solid coexistence lines, eutectic points, and critical points (as shown in Figs. 1, 7, and 8). In addition, the lattice constant R is assumed to be linearly proportional to ψ, i.e., the solute expansion satisfies Vegard's law. Details of the parameters entering this model are described in Ref. [18]. Here, α is the solute expansion coefficient and to further simply calculations, it will be assumed to be small. This approximation is valid for systems in which the relative size difference in the atomic species is small. In this limit, the free energy can be rewritten as

$$F = \int d\vec{x} \left[\frac{n}{2}(\Lambda^0 + \alpha\psi\Lambda^1)n - \frac{t}{3}n^3 + \frac{v}{4}n^4 + \gamma\psi + \frac{\omega}{2}\psi^2 + \frac{u}{4}\psi^4 + \frac{K}{2}|\vec{\nabla}\psi|^2 \right], \tag{3}$$

where

$$\Lambda^0 \equiv \Delta B_0 + B_2^\ell \psi^2 + B_0^x (1 + \nabla^2)^2,$$

$$\Lambda^1 \equiv 4B_0^x (\nabla^2 + \nabla^4), \tag{4}$$

$\Delta B_0 \equiv B_0^\ell - B_0^x$, $F \equiv \Delta\mathcal{F}/(k_B T \rho_\ell R_o^d)$, $\vec{x} \equiv \vec{r}/R_o$, and $K \equiv K'/R_o^2$. The equations of motion are then

$$\frac{\partial n}{\partial t} = \nabla^2\left[\Lambda^0 n - tn^2 + vn^3 + \frac{\alpha}{2}(\psi\Lambda^1 n + \Lambda^1 n\psi)\right], \quad (5)$$

$$\frac{\partial \psi}{\partial t} = \nabla^2\left[(\omega + n^2 B_2^\ell - K\nabla^2)\psi + u\psi^3 + \frac{\alpha}{2}n\Lambda^1 n\right], \quad (6)$$

where a time scale $Mk_BT\rho_\ell R_o^d$ has been adopted for the rescaling.

In the following section, the equations of motion will be developed for the slowly varying amplitudes that describe various crystalline systems. More formally, for any given periodic structure, the density field can be expanded as

$$n = n_0 + \sum_{\vec{G}_j} \eta_j \exp(i\vec{G}_j \cdot \vec{r}) + \sum_{\vec{G}_j} \eta_j^* \exp(-i\vec{G}_j \cdot \vec{r}), \quad (7)$$

which separates the "slow"-scale complex amplitudes η_j and average density field n_0 from the underlying small-scale crystalline structure that is characterized by $\vec{G}_j = l\vec{q}_1 + m\vec{q}_2 + n\vec{q}_3$, where $(\vec{q}_1, \vec{q}_2, \vec{q}_3)$ are the principle reciprocal-lattice vectors, (l,m,n) are integers, and the subscript j schematic refers to a specific set of (l,m,n). This particular parameterization implicitly assumes that a substitutional alloy is being considered, consistent with solutions that minimize both Eqs. (2) and (3). This analysis does not apply to more complicated ordered or superlattices structures. Since the equilibrium solutions of Eq. (2) for n are relatively smooth, only a few amplitudes in Eq. (7) are required. In what follows, model equations will be developed for only the lowest-order amplitudes that are needed to reconstruct a given crystal symmetry and defect structures relevant for controlling elastic and plastic effects in solidification and impurity segregation.

Recently, many efforts have been devoted to developing amplitude expansion for various physical systems. The central assumption of these approaches is that the amplitudes vary on scales much larger that the short (or "fast") atomic spacing scale. Formally, a small parameter can then be introduced that represents the ratio of the two scales and an expansion in this variable can be performed. To apply this analysis to Eqs. (5) and (6), both the amplitudes (η_j) and concentration field ψ are assumed to be slow variables (for technical details of this multiple-scale analysis, the reader can refer to Yeon *et al.* [31] and the references therein). For simplicity, in this paper, the average atomic density (i.e., n_0) will be assumed as constant and zero, since miscibility gaps between liquid and solid phases can be accounted for (to some extent) by a miscibility in ψ. Moreover, noise dynamics will be neglected here. More complete analysis involving dynamic variation of n_0, noise effects, as well as the general case of different atomic mobilities will be presented elsewhere [42].

III. AMPLITUDE EXPANSION FOR TRIANGULAR SYMMETRY

In two dimensions, the free energy given in Eq. (3) is minimized by a triangular lattice. The corresponding principle reciprocal-lattice vectors are given by

$$\vec{q}_1 = q_{eq}(-\hat{x} - 1/\sqrt{3}\hat{y}), \quad \vec{q}_2 = q_{eq}(2/\sqrt{3}\hat{y}), \quad (8)$$

where $q_{eq} = \sqrt{3}/2$ is the equilibrium wave number. To construct the minimal model of a triangular lattice, only the lowest-order reciprocal-lattice vectors are needed, which correspond to $\vec{q}_1$, $\vec{q}_2$, and $\vec{q}_3 \equiv -\vec{q}_1 - \vec{q}_2 = q_{eq}(\hat{x} - 1/\sqrt{3}\hat{y})$. To obtain equations of motion for the amplitudes of these lowest-order reciprocal-lattice vectors, a standard method of multiple-scale expansion [43] can be employed in the limit of small $\epsilon = -\Delta B_0 / B_0^x$. In such an expansion, the slowly varying amplitudes and concentration field are written as a function of the slowly varying scales, i.e., $(X,Y,T) = (\epsilon^{1/2}x, \epsilon^{1/2}y, \epsilon t)$. The next step is to expand η_j and ψ in a power series in $\epsilon^{1/2}$, substitute them into Eqs. (5) and (6), and obtain dynamical equations at each order of ϵ. Using a standard solvability condition [43] to solve these equations for complex amplitudes of only the lowest-order reciprocal vectors and to all orders in ϵ [31,42] leads to the following equations of motion:

$$\frac{\partial \eta_j}{\partial t} = \mathcal{L}_j\left\{[\Lambda_j^0 + 3v(A^2 - |\eta_j|^2)]\eta_j - 2t\prod_{i\neq j}\eta_i^* + \frac{\alpha}{2}(\psi\Lambda_j^1\eta_j + \Lambda_j^1\eta_j\psi)\right\},$$

$$\frac{\partial \psi}{\partial t} = \nabla^2\left[(w + B_2^\ell A^2 - K\nabla^2)\psi + u\psi^3 + \frac{\alpha}{2}\sum_j(\eta_j[\Lambda_j^1]^*\eta_j^* + \eta_j^*\Lambda_j^1\eta_j)\right], \quad (9)$$

where

$$\Lambda_j^0 \equiv \Delta B_0 + B_2^\ell\psi^2 + B_0^x(\mathcal{G}_j)^2,$$

$$\Lambda_j^1 \equiv 4B_0^x\mathcal{L}_j\mathcal{G}_j,$$

$$\mathcal{L}_j \equiv \nabla^2 + 2i\vec{q}_j\cdot\vec{\nabla} - |\vec{q}_j|^2,$$

$$\mathcal{G}_j \equiv \nabla^2 + 2i\vec{q}_j\cdot\vec{\nabla},$$

$$A^2 \equiv 2\sum_{j=1}^{3}|\eta_j|^2. \quad (10)$$

To further simplify calculations, a long-wavelength approximation will be made such that $\mathcal{L}_j \approx -|\vec{q}_j|^2 = -1$. Unfortunately, a similar long-wavelength approximation cannot be made for $\mathcal{G}_j$ (e.g., replacing $\mathcal{G}_j$ by $2i\vec{q}_j\cdot\vec{\nabla}$) as then the equations would not be rotationally invariant. The rotational invariance of these equations is straightforward to show using the procedure described in Ref. [44], which shows that the full operator $\mathcal{G}_j$ is required to preserve rotational symmetry and lead to equivariant amplitude equations for a specified set of base wave vectors $\vec{q}_j$. In this long-wavelength limit, the equations of motion become

$$\frac{\partial \eta_j}{\partial t} = -\left\{ [\Delta B_0 + B_2^\ell \psi^2 + B_0^x \mathcal{G}_j^2 + 3v(A^2 - |\eta_j|^2)]\eta_j - 2t\prod_{i\neq j} \eta_i^* - 2\alpha B_0^x(\psi \mathcal{G}_j \eta_j + \mathcal{G}_j \eta_j \psi) \right\},$$

$$\frac{\partial \psi}{\partial t} = \nabla^2 \left[(w + B_2^\ell A^2 - K\nabla^2)\psi + u\psi^3 - 2B_0^x \alpha \sum_j (\eta_j \mathcal{G}_j^* \eta_j^* + \eta_j^* \mathcal{G}_j \eta_j) \right]. \quad (11)$$

These dynamics can alternatively be written in a form of model C type (in the Halperin-Hohenberg classification scheme [45]), i.e.,

$$\frac{\partial \eta_j}{\partial t} = -\frac{\delta F}{\delta \eta_j^*}, \quad \frac{\partial \psi}{\partial t} = \nabla^2 \frac{\delta F}{\delta \psi}, \quad (12)$$

where

$$F = \int d\vec{r} \left[\frac{\Delta B_0}{2} A^2 + \frac{3v}{4} A^4 + \sum_{j=1}^{3} \left\{ B_0^x |\mathcal{G}_j \eta_j|^2 - \frac{3v}{2} |\eta_j|^4 \right\} - 2t\left(\prod_{j=1}^{3} \eta_j + \text{c.c.} \right) + (\omega + B_2^\ell A^2)\frac{\psi^2}{2} + \frac{u}{4}\psi^4 + \frac{K}{2}|\vec{\nabla}\psi|^2 - 2B_0^x \alpha \sum_{j=1}^{3} (\eta_j \mathcal{G}_j^* \eta_j^* + \text{c.c.})\psi \right], \quad (13)$$

with c.c. referring to the complex conjugate.

A. Small deformation limit

To gain insight into the above results and make connection with traditional phase-field models, it is useful to rewrite η_j in the form $\eta_j = \phi e^{i\vec{q}_j \cdot \vec{u}}$. In this case, the magnitude of ϕ distinguishes between liquid ($\phi = 0$) and solid phases ($\phi \neq 0$), while $\vec{u}$ is the displacement vector introduced in continuum elasticity theory [48] to describe displacement of atoms from a perfectly ordered crystal lattice. To make a connection with standard phase-field models, this expression is first substituted into Eq. (13) and then Eq. (13) is expanded up to the lowest-order nontrivial gradients in ϕ, ψ, and $\vec{u}$. This calculation gives

$$F = \int d\vec{r} \left[\left\{ 3\Delta B_0 \phi^2 - 4t\phi^3 + \frac{45}{2} v\phi^4 + (\omega + 6B_2^\ell \phi^2)\frac{\psi^2}{2} + \frac{u}{4}\psi^4 \right\} + \left\{ \frac{K}{2}|\vec{\nabla}\psi|^2 + 6B_0^x |\vec{\nabla}\phi|^2 \right\} + 3B_0^x \left\{ \sum_{i=1}^{2} \left(\frac{3}{2} U_{ii}^2 \right) + U_{xx}U_{yy} + 2U_{xy}^2 \right\} \phi^2 + 12\alpha B_0^x \left\{ -\phi\nabla^2\phi + \sum_{i=1}^{2} U_{ii}\phi^2 \right\} \psi \right], \quad (14)$$

where $U_{ij} \equiv (\partial u_i/\partial x_j + \partial u_j/\partial x_i)/2$ is the linear strain tensor. The first set of terms (defined by the $\{\ldots\}$ brackets) is remarkably similar to standard phase-field models developed for eutectic and dendritic solidifications [46,47]. The polynomial in ϕ gives a first-order transition from a liquid ($\phi = 0$) to solid phase ($\phi \neq 0$). The polynomial in ψ is the typical "ψ^4" free energy used in the Cahn-Hilliard-Cook-type models. The coupling term $\phi^2\psi^2$ (note: B_2^ℓ is negative) can lead to phase segregation at low temperatures when ϕ becomes large. The second and third sets of terms account for surface and linear elastic energies, respectively. From the form of the third term, it is straightforward [48] to derive the elastic constants in dimensionless units, i.e., $C_{11} = C_{22} = 9B_0^x\phi^2$ and $C_{12} = C_{44} = C_{11}/3$.

Finally, the last set of terms couples the concentration field to the liquid-solid order parameter ϕ when the atomic species have a different size (i.e., $\alpha \neq 0$). The term, $\psi\phi\nabla^2\phi$, implies preferential phase segregation to liquid-solid surfaces, grain boundaries, and dislocations (i.e., regions in which ϕ varies in space). Dynamically, this term is responsible for solute migration at grain boundaries and solute drag. The last term $\psi\phi^2(U_{xx} + U_{yy})$ implies a coupling between strain and concentration as should be expected when the atomic species have different sizes. It may appear unusual that the free-energy functional depends on the sign of the displacement gradients (via $U_{xx} = \partial u_x/\partial x$); however, this sign determines whether there is a local compression or expansion of the lattice which would favor a specific atomic species based on the sign of solute expansion coefficient α.

B. Equilibrium phase diagram

The equilibrium phase diagram can be evaluated to lowest order by considering ϕ and ψ constant and a bulk compression to account for solute expansion, such that $\vec{u} \equiv \delta(x\hat{x} + y\hat{y})$. In this limit, the free energy per unit area ($\mathcal{A}$) becomes

$$\frac{F}{\mathcal{A}} = 3\Delta B_0 \phi^2 - 4t\phi^3 + \frac{45}{2} v\phi^4 + \frac{u}{4}\psi^4 + (\omega + 6B_2^\ell \phi^2)\frac{\psi^2}{2} + 12B_0^x \phi^2(\delta^2 + 2\alpha\psi\delta). \quad (15)$$

Minimizing with respect to δ gives $\delta_{eq} = -\alpha\psi$. As expected, the contraction or expansion of the lattice is controlled by $\alpha\psi$. Substituting δ_{eq} for δ leads to

$$\frac{F}{\mathcal{A}} = 3\Delta B_0 \phi^2 - 4t\phi^3 + \frac{45}{2} v\phi^4 + (\omega + 6B_2^\ell \phi^2)\frac{\psi^2}{2} + \frac{u}{4}\psi^4 - 12B_0^x(\phi\alpha\psi)^2, \quad (16)$$

which is then minimized with respect to ϕ, yielding

$$\phi_{eq} = \frac{t + \sqrt{t^2 - 15v[\Delta B_0 + \psi^2(B_2^\ell - 4B_0^x\alpha^2)]}}{15v}. \quad (17)$$

Substituting Eq. (17) into Eq. (16) yields a free energy per unit area that is only a function of ψ. This result can be used to construct the phase diagram in an analogous manner as was done in Ref. [18]. Two example phase diagrams and the corresponding model parameters required to obtain each are shown in Fig. 1.

The derivation of amplitude equations and the related simplifications presented above can be readily extended to three-dimensional systems. In Appendixes A and B, the rel-

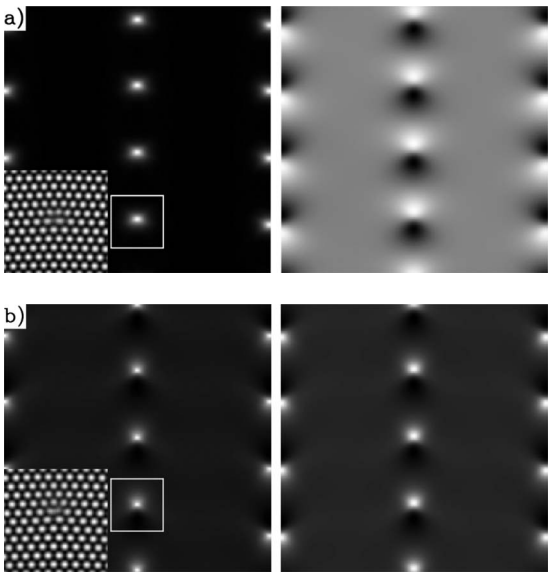

FIG. 2. Solute segregations in symmetric grain boundaries with misorientation $\theta=3.76°$ are shown for $\psi=0$ (a) and $\psi=0.2$ (b). Left and right panels correspond to $\Sigma_j|\eta_j|^2$ and ψ, respectively. In the corner insets of left panels, the density field n is reconstructed from the amplitudes η_j for the boxed region. In the right panels, the dark (light) color corresponds to the larger (smaller) of the atomic species. The parameters for (a) and (b) correspond to Figs. 1(a) and 1(b) at $\Delta B_0=0.01$, respectively. The dimension of each panel is $55a\times 55a$, where a is the lattice constant.

evant equations and sample phase diagrams for both bcc and fcc symmetries are presented.

IV. APPLICATIONS

To further examine the above amplitude equations, numerical simulations of the model described by Eqs. (12) and (13) were undertaken and the results are shown in Figs. 2–6. In Fig. 2, simulations were conducted to study the coupling between composition and topological defects (dislocations and grain boundaries) in binary alloys with components of different atomic sizes, i.e., nonzero solute expansion coefficient α. For this study, a symmetric tilt grain boundary between two grains with a misorientation angle of $\theta=3.76°$ was created by dynamically evolving an initial configuration of two perfect crystals separated by a layer of supercooled liquid. As time evolves, the liquid solidifies and a grain boundary spontaneously forms. The dislocation cores that comprise the grain boundary interact with the different atomic species or alloy composition. As shown in Fig. 2, the larger (smaller) solute atoms preferentially segregate around the dislocation cores in regions of tensile (compressive) strain. This preferentially segregation around dislocation cores has been observed directly in experiments [49,50] and is usually referred to as a Cottrell atmosphere after Cottrell and Bilby [51].

Simulation results for eutectic solidification and phase separation are presented in Fig. 3, where three small grains of different orientations are heterogeneously nucleated for the parameters used in Fig. 1(b) and for a "temperature" ΔB_0 below the eutectic point. As the grains grow, lamellar concentration bands form within the grains as a result of phase separation. The formation of such lamellar structures is a well-known phenomenon that has been observed in many experiments and theoretical studies [46,47,52–55]. The relatively large lattice mismatch (roughly 8.4% in equilibrium due to a finite solute expansion coefficient) between the lamellae results in the spontaneous nucleation of dislocation at the lamellar interfaces. It is reasonable to assume that the misfit strains and the dislocation nucleation between lamellae will modify the spacing selection mechanism predicted by previous eutectic solidification theories [52,53]. The collec-

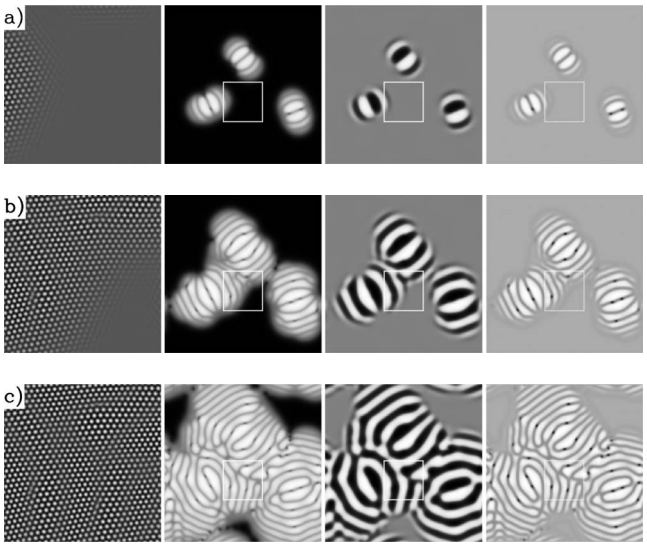

FIG. 3. Eutectic solidification for parameters in Fig. 1(b) at $\Delta B_0=0.022$ and $\psi=0.0$. Panels (a), (b), and (c) correspond to dimensionless times 30 000, 60 000, and 105 000, respectively. From left to right, the columns correspond to n reconstructed from η_j (for the boxed region), $\Sigma_j|\eta_j|^2$, ψ, and the local free-energy density. Dislocations are most easily identified as small black dots in the local free-energy density. The sizes of the panels are $27.5a\times 27.5a$ and $110a\times 110a$ in the first column and last three columns respectively, where a is the lattice constant.

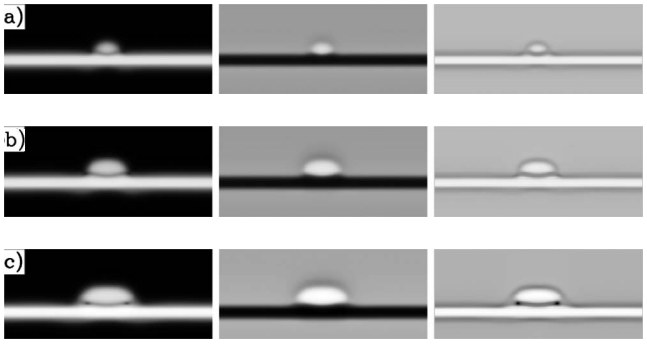

FIG. 4. Quantum dot formation on a 5-atomic-layer-thick nanomembrane at times $t=20\,000$, 60 000, and 100 000 [for (a), (b), and (c), respectively]. The columns from left to right correspond to $\Sigma|\eta_j|^2$, ψ, and the local free-energy density. The parameters used for this simulation are from Fig. 1(a) except $\alpha=0.26$ and $B_0^\ell=1.028$. Each $122a\times 53a$ panel shown is a portion of the full $122a\times 211a$ simulation cell, where a is the lattice constant of the unstrained film.

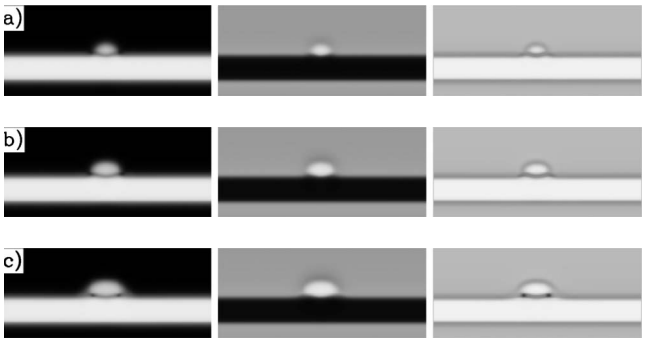

FIG. 5. Quantum dot formation on a 12-atomic-layer-thick nanomembrane at times $t=20\,000$, 40 000, and 60 000 [for (a), (b), and (c), respectively]. The parameters used and system size are identical to those in Fig. 4.

tion of dislocations at such interfaces has been reported in other studies [56] and is expected to alter the concentration segregation rate. When the grains impinge on one another (i.e., coarsening occurs), additional dislocations form, leading to complex patterns as shown in Figs. 3(b) and 3(c). These simulations indicate that the amplitude model established here can simultaneously describe the complex evolution of liquid-solid interfaces, grain boundaries, dislocations, and interfaces between regions of different compositions.

Numerical simulations were also conducted to study islands or quantum dots formation on thin freely standing films or solid nanomembranes. Recent experiments of Ge on Si membranes [57,58] have suggested that growth on such nanomembranes strongly influences the maximum size that the strained islands can form coherently (i.e., without dislocations) and can lead to correlation or self-ordering of multiple islands. To examine this phenomenon, simulations were set up such that islands of one material were grown on a thin free-standing membrane of another material by exploiting a eutectic phase diagram [such as that shown in Fig. 1(b)]. To initiate growth of the islands, a small crystal region at $\psi=-0.12$ was constructed coherently on top of a thin membrane at $\psi=0.2$ in a supercooled liquid at $\psi=-0.03$, with ΔB set to be 0.028. Sample simulation results are shown in Figs. 4 and 5. As can be seen in these figures, the dot grows coherently with the membrane until reaching some critical size at which dislocations are nucleated at the liquid-dot-membrane junction. Perhaps, more interestingly by comparing Figs. 4 and 5, it is apparent that for the thinner membrane, the dots can grow to a larger size before nucleating dislocations. This result occurs as the strained quantum dots partially relax by straining the substrate membrane and thinner membranes are easier to deform than thicker ones. Such mechanism has been proved to play an important role in engineering the self-assembly of thin-film nanostructures such as quantum dots [57].

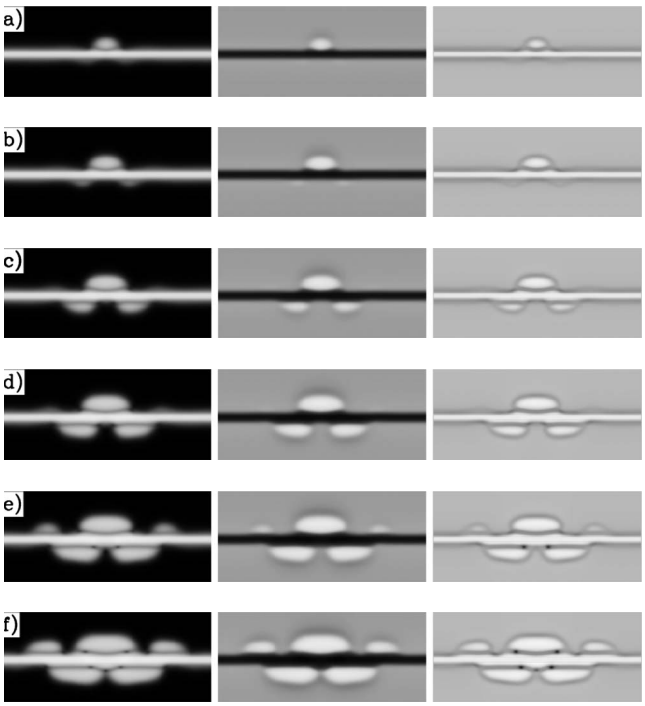

FIG. 6. Correlated quantum dot formation on a 3-atomic-layer-thick nanomembrane at times $t=20\,000$, 40 000, 60 000, 80 000, 100 000, and 120 000 [for (a)–(f), respectively]. The parameters used and system size are identical to those in Fig. 4 except for a higher liquid supersaturation.

Another interesting consequence of the membrane deformation is that it locally creates favorable and unfavorable positions for the nucleation of other islands or dots, with an alternative sequence on the two sides of the membrane, as can be seen in Fig. 6 which was conducted at a higher liquid supersaturation (i.e., $\psi=-0.04$) or growth rate. Once a dot is formed, e.g., on the top of the membrane, it is preferable for the next ones to nucleate under the edges rather than directly underneath the top quantum dot. After these bottom-side dots are formed, they in turn create preferential regions for a new set of dots to nucleate on the top (above their edges) and the process repeats. In such a fashion, the process leads to the correlated dot growth as observed in experiments of Ge or SiGe islands on Si membranes [57,58]. This phenomenon can in principle be exploited to create periodic strained nanostructures that in turn produce periodically modulated band gaps.

Finally, it should be noted that in the dynamics described by Eq. (12), the diffusion constant for the concentration field (ψ) is similar in magnitude in the liquid and solid phases. However, it is typically the case that diffusion or atomic mobility in liquids is much larger than in solids. In most traditional phase-field models of binary-alloy solidification, this difference is modeled by making the mobility depend on the order parameter (i.e., phase-field) as well as the concentration [60–62]. A similar approach can be taken for the amplitude equations by using the following dynamic equation for ψ:

$$\frac{\partial \psi}{\partial t} = \vec{\nabla} \cdot \left(M(A,\psi) \vec{\nabla} \frac{\delta F}{\delta \psi} \right), \tag{18}$$

where the mobility now depends on $A^2=\Sigma_j |\eta_j|^2$. The following functional form:

$$M(A,\psi) = M_X(\psi) + (M_L(\psi) - M_X(\psi))[1 - \tanh(aA)], \tag{19}$$

Would, for example, change M from the mobility of the crystal (M_X) at large aA to the mobility in the liquid phase (M_L) at small or zero aA. The parameter a would control how quickly the M changes from liquid to solid phases. Note that while the binary PFC model presented in Eq. (1) assumes both atomic species have the same mobility, the individual phase mobilities M_x and M_L are concentration dependent.

V. DISCUSSIONS AND CONCLUSIONS

In this paper, amplitude equations have been derived from the binary phase-field-crystal model for a two-dimensional triangular lattice and for three-dimensional bcc and fcc structures. Furthermore, the connection to standard phase-field models has been established and for small deformations, the results have been shown to recover linear continuum elasticity theory and reconstruct the equilibrium phase diagrams for binary-alloy systems. Sample simulations of the amplitude equations have shown that this relatively simple model can effectively model many complex phenomena and the emergent microstructures that arise and reveal the underlying mechanisms. While these amplitude equations were derived from an atomistic model, they can in themselves be regarded as phase-field models with complex order parameters. One advantage of this amplitude description is that the liquid and solid phases are easily distinguished by a relative uniform quantity $A^2 \equiv \Sigma_j |\eta_j|^2$ and the coupling and interaction between structure (i.e., amplitudes) and concentration can be well identified. In this regard, it may be possible to extend the equations to naturally incorporate other uniform fields, such as magnetization, polarization, temperature, etc., and simultaneously include elastic and plastic deformations in polycrystalline samples.

ACKNOWLEDGMENTS

K.R.E. acknowledges support from NSF under Grant No. DMR-0906676. Z.-F.H. acknowledges support from NSF under Grant No. CAREER DMR-0845264. N.P. acknowledges support from the National Science and Engineering Research Council of Canada.

APPENDIX A: AMPLITUDE EQUATIONS FOR BCC SYMMETRY

For a bcc lattice, the principle reciprocal-lattice vectors are

$$\vec{q}_1 = q_{eq}(\hat{x} + \hat{y}),$$

$$\vec{q}_2 = q_{eq}(\hat{x} + \hat{z}),$$

$$\vec{q}_3 = q_{eq}(\hat{y} + \hat{z}), \tag{A1}$$

where $q_{eq} = 1/\sqrt{2}$ is the equilibrium wave number. In a one-mode approximation, the above principle reciprocal-lattice vectors need to be combined with the following vectors: $\vec{q}_4 = \vec{q}_1 - \vec{q}_2 = q_{eq}(\hat{y} - \hat{z})$, $\vec{q}_5 = \vec{q}_2 - \vec{q}_3 = q_{eq}(\hat{x} - \hat{y})$, and $\vec{q}_6 = \vec{q}_3 - \vec{q}_1 = q_{eq}(-\hat{x} + \hat{z})$. Thus, the bcc structure can be represented in the usual manner, i.e.,

$$n = \sum_{j=1}^{j=6} \eta_j(\vec{r},t)\exp(i\vec{q}_j \cdot \vec{r}) + \sum_{j=1}^{j=6} \eta_j^*(\vec{r},t)\exp(-i\vec{q}_j \cdot \vec{r}). \tag{A2}$$

Repeating the calculations presented in Sec. III (with the same level of approximations) gives the following complex amplitude equations:

$$\frac{\partial \eta_1}{\partial t} = -\{[\Delta B_0 + B_0^x \mathcal{G}_1^2 + 3v(A^2 - |\eta_1|^2)]\eta_1 - 2t(\eta_3\eta_6^* + \eta_2\eta_4) + 6v(\eta_3\eta_4\eta_5 + \eta_2\eta_5^*\eta_6^*) - 2\alpha B_0^x(\psi\mathcal{G}_1\eta_1 + \mathcal{G}_1\eta_1\psi)\}, \tag{A3}$$

$$\frac{\partial \eta_4}{\partial t} = -\{[\Delta B_0 + B_0^x \mathcal{G}_4^2 + 3v(A^2 - |\eta_4|^2)]\eta_4 - 2t(\eta_5^*\eta_6^* + \eta_1\eta_2^*) + 6v(\eta_1\eta_3^*\eta_5^* + \eta_3\eta_2^*\eta_6^*) - 2\alpha B_0^x(\psi\mathcal{G}_4\eta_4 + \mathcal{G}_4\eta_4\psi)\}, \tag{A4}$$

with equations of motion for η_2 and η_3 obtained by cyclic permutations on the groups (1,2,3) and (4,5,6) in Eq. (A3), while equations for η_5 and η_6 can be obtained by the similar cyclic permutations of Eq. (A4). The corresponding concentration equation is given by

$$\frac{\partial \psi}{\partial t} = \nabla^2\left((w + B_2^\ell A^2 - K\nabla^2)\psi + u\psi^3 - 2B_0^x\alpha\sum_j [\eta_j\mathcal{G}_j^*\eta_j^* + \eta_j^*\mathcal{G}_j\eta_j]\right). \tag{A5}$$

Once again, Eqs. (A3)–(A5) can be rewritten in a model C–type form, i.e.,

$$\frac{\partial \eta_j}{\partial t} = -\frac{\delta F}{\delta \eta_j^*}, \quad \frac{\partial \psi}{\partial t} = \nabla^2 \frac{\delta F}{\delta \psi}, \tag{A6}$$

where

$$F = \int d\vec{r}\left[\frac{\Delta B_0}{2}A^2 + \frac{3v}{4}A^4 + \sum_{j=1}^{6}\left\{B_0^x|\mathcal{G}_j\eta_j|^2 - \frac{3v}{2}|\eta_j|^4\right\} + 6v(\eta_1\eta_3^*\eta_4^*\eta_5^* + \eta_2\eta_1^*\eta_5^*\eta_6^* + \eta_3\eta_2^*\eta_6^*\eta_4^* + \text{c.c.}) - 2t([\eta_1^*\eta_2\eta_4 + \eta_2^*\eta_3\eta_5 + \eta_3^*\eta_1\eta_6 + \text{c.c.}] + [\eta_4^*\eta_5^*\eta_6^* + \text{c.c.}]) - 2B_0^x\alpha\sum_{j=1}^{6}(\eta_j\mathcal{G}_j^*\eta_j^* + \eta_j^*\mathcal{G}_j\eta_j)\psi + (\omega + B_2^\ell A^2)\frac{\psi^2}{2} + \frac{u}{4}\psi^4 + \frac{K}{2}|\vec{\nabla}\psi|^2\right]. \tag{A7}$$

As discussed in Sec. III A, it is interesting to replace η_j by $\phi\exp(i\vec{q}_j\cdot\vec{r})$, yielding

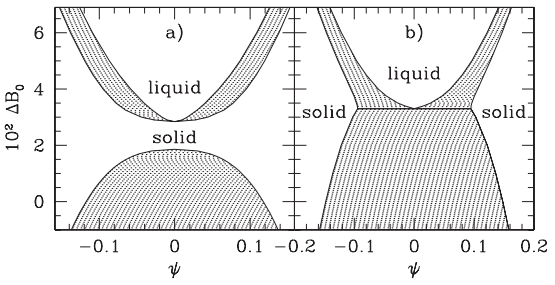

FIG. 7. Sample phase diagram for three-dimensional bcc system with same parameter set and notation as in Fig. 1 except $\omega=0.05$ in (a).

$$F=\int d\vec{r}\Bigg[\Bigg\{6\Delta B_0\phi^2-16t\phi^3+135v\phi^4+(\omega+12B_2^\ell\phi^2)\frac{\psi^2}{2}+\frac{u}{4}\psi^4\Bigg\}-\Bigg\{\frac{K}{2}\psi\nabla^2\psi+8B^x(1+3\alpha\psi)\phi\nabla^2\phi\Bigg\}+4B_0^x\Bigg\{\sum_{i=1}^{3}\Bigg(U_{ii}^2+4\alpha\psi U_{ii}+\frac{1}{2}\sum_{j\neq i}^{3}U_{ii}U_{jj}\Bigg)+2\sum_{i=4}^{6}U_{ii}^2\Bigg\}\phi^2\Bigg]. \tag{A8}$$

Similarly, the elastic constants can be derived as $C_{11}=C_{22}=C_{33}=8B_0^x\phi^2$ and $C_{12}=C_{13}=C_{23}=C_{44}=C_{55}=C_{66}=C_{11}/2$. Furthermore, minimizing with respect to δ gives $\delta_{eq}=-\alpha\psi$, which leads to the following result for the free energy per unit volume:

$$\frac{F}{\mathcal{V}}=6\Delta B_0\phi^2-16t\phi^3+135v\phi^4+(\omega+6B_2^\ell\phi^2)\frac{\psi^2}{2}+\frac{u}{4}\phi^4-24B_0^x(\alpha\psi\phi)^2, \tag{A9}$$

which can be minimized with respect to ϕ to obtain

$$\phi_{eq}=\frac{2t+\sqrt{4t^2-45v(\Delta B_0+\psi^2(B_2^\ell-4B_0^x\alpha^2)}}{45v}. \tag{A10}$$

The corresponding phase diagram for this model is shown in Fig. 7.

APPENDIX B: AMPLITUDE EQUATIONS FOR FCC SYMMETRY

Recently, Wu [59] showed that the basic phase-field crystal model can be extended to model a fcc lattice by including an extra length scale. Replacing the operator $\Delta B+B^x(1+R^2\nabla^2)^2\rightarrow\mathcal{D}\equiv\Delta B+16B^x(1+2R_1^2\nabla^2+R_1^4\nabla^4)(1+2R_2^2\nabla^2+R_2^4+E)$, where $R_2=\sqrt{3}/2R_1$ for a fcc lattice and the extra factor of 16 is introduced just for convenience, gives a revised alloy PFC free energy

$$F=\int d\vec{r}\Bigg\{\frac{n\mathcal{D}n}{2}-\frac{t}{3}n^3+\frac{v}{4}n^4+\frac{\omega}{2}\psi^2+\frac{u}{4}\psi^4+\frac{K}{2}|\vec{\nabla}\psi|^2\Bigg\}. \tag{B1}$$

Here, the parameter E controls the symmetry of the phase such that for large (small) E, a bcc (fcc) structure is favored. The following calculations focus on the fcc phase in the limit of $E=0$. Furthermore, to examine the influence of solute expansion, the parameters R_1 and R_2 can be set to be $R_1=1+\alpha\psi$ and $R_2=\sqrt{3}/2(1+\alpha\psi)$. In the small $\alpha\psi$ limit, the free-energy functional becomes

$$F=\int d\vec{r}\Bigg\{\frac{n\Lambda^0 n}{2}+\alpha\psi\frac{n\Lambda^1 n}{2}-\frac{t}{3}n^3+\frac{v}{4}n^4+\frac{\omega}{2}\psi^2+\frac{u}{4}\psi^4+\frac{K}{2}|\vec{\nabla}\psi|^2\Bigg\}, \tag{B2}$$

showing the same form as Eq. (3) but with different operators

$$\Lambda^0\equiv\Delta B_0+B_2^\ell\psi^2+16B^x(1+\nabla^2)^2(1+3/4\nabla^2)^2,$$

$$\Lambda^1\equiv 16B^x\nabla^2(1+\nabla^2)(1+3/4\nabla^2)(7+6\nabla^2). \tag{B3}$$

The corresponding equations of motion are also governed by Eqs. (5) and (6), with Λ^0 and Λ^1 given above.

For the fcc symmetry, the principle reciprocal-lattice vectors are

$$\vec{q}_1=q_{eq}(-\hat{x}+\hat{y}+\hat{z})/\sqrt{3},$$

$$\vec{q}_2=q_{eq}(\hat{x}-\hat{y}+\hat{z})/\sqrt{3},$$

$$\vec{q}_3=q_{eq}(\hat{x}+\hat{y}-\hat{z})/\sqrt{3}. \tag{B4}$$

To construct a fcc crystal, the following reciprocal-lattice vectors are also required:

$$\vec{q}_4=-\vec{q}_1-\vec{q}_2-\vec{q}_3=q_{eq}(-\hat{x}-\hat{y}-\hat{z})/\sqrt{3},$$

$$\vec{q}_5=\vec{q}_1+\vec{q}_2=2q_{eq}\hat{z}/\sqrt{3},$$

$$\vec{q}_6=\vec{q}_2+\vec{q}_3=2q_{eq}\hat{x}/\sqrt{3},$$

$$\vec{q}_7=\vec{q}_3+\vec{q}_1=2q_{eq}\hat{y}/\sqrt{3}. \tag{B5}$$

Unlike the triangular and bcc symmetries, the fcc lattice requires at minimum two sets of vectors of different lengths, i.e., $(\vec{q}_1,\vec{q}_2,\vec{q}_3,\vec{q}_4)$ with length q_{eq} and $(\vec{q}_5,\vec{q}_6,\vec{q}_7)$ with length $2/\sqrt{3}q_{eq}$. The density field n is then expanded in the usual fashion, i.e.,

$$n=\sum_{j=1}^{j=7}\eta_j(\vec{r},t)\exp(i\vec{q}_j\cdot\vec{r})+\text{c.c.} \tag{B6}$$

Following the standard procedure, the amplitude equations can be derived as

$$\frac{\partial \eta_1}{\partial t} = \mathcal{L}_1\Big[\Lambda_1^0\eta_1 - 2t(\eta_2^*\eta_5 + \eta_3^*\eta_7 + \eta_4^*\eta_6^*) + 6v(\{A^2 - |\eta_1|^2/2\}\eta_1 + \eta_2^*\eta_3^*\eta_4^* + \eta_2\eta_6^*\eta_7 + \eta_3\eta_5\eta_6^* + \eta_4\eta_5\eta_7) + \frac{\alpha}{2}(\psi\Lambda_1^1\eta_1 + \Lambda_1^1\eta_1)\Big], \tag{B7}$$

$$\frac{\partial \eta_2}{\partial t} = \mathcal{L}_2\Big[\Lambda_2^0\eta_2 - 2t(\eta_3^*\eta_6 + \eta_4^*\eta_7^* + \eta_1^*\eta_5) + 6v(\{A^2 - |\eta_2|^2/2\}\eta_2 + \eta_1^*\eta_3^*\eta_4^* + \eta_1\eta_6\eta_7^* + \eta_3\eta_5\eta_7^* + \eta_4\eta_5\eta_6) + \frac{\alpha}{2}(\psi\Lambda_2^1\eta_2 + \Lambda_2^1\eta_2)\Big], \tag{B8}$$

$$\frac{\partial \eta_3}{\partial t} = \mathcal{L}_3\Big[\Lambda_3^0\eta_3 - 2t(\eta_4^*\eta_5^* + \eta_1^*\eta_7 + \eta_2^*\eta_6) + 6v(\{A^2 - |\eta_3|^2/2\}\eta_3 + \eta_1^*\eta_2^*\eta_4^* + \eta_1\eta_5^*\eta_6 + \eta_2\eta_5^*\eta_7 + \eta_4\eta_6\eta_7) + \frac{\alpha}{2}(\psi\Lambda_3^1\eta_3 + \Lambda_3^1\eta_3)\Big], \tag{B9}$$

$$\frac{\partial \eta_4}{\partial t} = \mathcal{L}_4\Big[\Lambda_4^0\eta_4 - 2t(\eta_1^*\eta_6^* + \eta_2^*\eta_7^* + \eta_3^*\eta_5^*) + 6v(\{A^2 - |\eta_4|^2/2\}\eta_4 + \eta_1^*\eta_2^*\eta_3^* + \eta_1\eta_5^*\eta_7^* + \eta_2\eta_5^*\eta_6^* + \eta_3\eta_6^*\eta_7^*) + \frac{\alpha}{2}(\psi\Lambda_4^1\eta_4 + \Lambda_4^1\eta_4)\Big], \tag{B10}$$

$$\frac{\partial \eta_5}{\partial t} = \mathcal{L}_5\Big[\Lambda_5^0\eta_5 - 2t(\eta_1\eta_2 + \eta_3^*\eta_4^*) + 6v(\{A^2 - |\eta_5|^2/2\}\eta_5 + \eta_6\eta_1\eta_3^* + \eta_6^*\eta_2\eta_4^* + \eta_7\eta_2\eta_3^* + \eta_7^*\eta_1\eta_4^*) + \frac{\alpha}{2}(\psi\Lambda_5^1\eta_5 + \Lambda_5^1\eta_5)\Big], \tag{B11}$$

$$\frac{\partial \eta_6}{\partial t} = \mathcal{L}_6\Big[\Lambda_6^0\eta_6 - 2t(\eta_2\eta_3 + \eta_4^*\eta_1^*) + 6v(\{A^2 - |\eta_6|^2/2\}\eta_6 + \eta_7\eta_2\eta_1^* + \eta_7^*\eta_3\eta_4^* + \eta_5\eta_3\eta_1^* + \eta_5^*\eta_2\eta_4^*) + \frac{\alpha}{2}(\psi\Lambda_6^1\eta_6 + \Lambda_6^1\eta_6)\Big], \tag{B12}$$

$$\frac{\partial \eta_7}{\partial t} = \mathcal{L}_7\Big[\Lambda_7^0\eta_7 - 2t(\eta_1\eta_3 + \eta_2^*\eta_4^*) + 6v(\{A^2 - |\eta_7|^2/2\}\eta_7 + \eta_5\eta_2^*\eta_3 + \eta_5^*\eta_1\eta_4^* + \eta_6\eta_1\eta_2^* + \eta_6^*\eta_3\eta_4^*) + \frac{\alpha}{2}(\psi\Lambda_7^1\eta_7 + \Lambda_7^1\eta_7)\Big], \tag{B13}$$

$$\frac{\partial \psi}{\partial t} = \nabla^2\Big((w + B_2^\ell A^2 - K\nabla^2)\psi + u\psi^3 + \frac{\alpha}{2}\sum_j[\eta_j(\Lambda_j^1)^*\eta_j^* + \eta_j^*\Lambda_j^1\eta_j]\Big), \tag{B14}$$

where $\mathcal{L}_j \equiv \nabla^2 + 2i\vec{q}_j\cdot\vec{\nabla} - |\vec{q}_j|^2$, $A^2 \equiv 2\Sigma_j|\eta_j|^2$, and

$$\Lambda_j^0 \equiv \Delta B_0 + B_2^\ell\psi^2 + 16B^x(1+\mathcal{L}_j)^2(1+3\mathcal{L}_j/4)^2,$$

$$\Lambda_j^1 \equiv 16B^x\mathcal{L}_j(1+\mathcal{L}_j)(1+3/4\mathcal{L}_j)(7+6\mathcal{L}_j). \tag{B15}$$

Note that $|\vec{q}_j|^2=1$ for $j=1,2,3,4$ and $|\vec{q}_j|^2=4/3$ for $j=5,6,7$ and thus

$$\Lambda_j^0 = \begin{cases} \Delta B_0 + B_2^\ell\psi^2 + B^x(\mathcal{G}_j)^2(3\mathcal{G}_j+1)^2 & j=1,2,3,4 \\ \Delta B_0 + B_2^\ell\psi^2 + B^x(3\mathcal{G}_j-1)^2(\mathcal{G}_j)^2 & j=5,6,7 \end{cases} \approx \Delta B_0 + B_2^\ell\psi^2 + B^x(\mathcal{G}_j)^2 \quad j=1,\ldots,7, \tag{B16}$$

$$\Lambda_j^1 = \begin{cases} 4^x(\mathcal{G}_j-1)\mathcal{G}_j(3\mathcal{G}_j+1)(6\mathcal{G}_j+1) & j=1,2,3,4 \\ 4B^x(\mathcal{G}_j-4/3)(3\mathcal{G}_j-1)\mathcal{G}_j(6\mathcal{G}_j-1) & j=5,6,7 \end{cases} \approx \begin{cases} -4B^x(\mathcal{G}_j) & j=1,2,3,4 \\ -4B^x(4\mathcal{G}_j/3) & j=5,6,7, \end{cases} \tag{B17}$$

where $\mathcal{G}_j \equiv \nabla^2 + 2i\vec{q}_j\cdot\vec{\nabla}$. Finally, as described in Sec. III A, the operator $\mathcal{L}_j$ acting on the right-hand side of each equation can be approximated by constants, i.e., $\mathcal{L}_j \approx -|\vec{q}_j|^2$. As before, the dynamical equations can be written as

$$\frac{\partial \eta_j}{\partial t} = -|\vec{q}_j|^2\frac{\delta F}{\delta \eta_j^*},$$

$$\frac{\partial \psi}{\partial t} = \nabla^2\frac{\delta F}{\delta \psi}, \tag{B18}$$

where

$$F = \int d\vec{r}\Big\{\frac{\Delta B_0}{2}A^2 + \frac{3v}{2}A^4 + \sum_{j=1}^{7}\Big(B^x|\mathcal{G}_j\eta_j|^2 - \frac{9v}{2}|\eta_j|^4\Big) - 2t[\eta_1^*(\eta_2^*\eta_5 + \eta_3^*\eta_7 + \eta_4^*\eta_6^*) + \eta_2^*(\eta_3^*\eta_6 + \eta_4^*\eta_7^*) + \eta_3^*\eta_4^*\eta_5^* + \text{c.c.}] + 6v[\eta_1^*(\eta_2^*\eta_3^*\eta_4^* + \eta_2\eta_6^*\eta_7 + \eta_3\eta_5\eta_6^* + \eta_4\eta_5\eta_7) + \eta_2^*\eta_5(\eta_3\eta_7^* + \eta_4\eta_6) + \eta_3^*\eta_4\eta_6\eta_7 + \text{c.c.}] - 2\alpha B_0^x\Big(\sum_{j=1}^{4}\eta_j^*\mathcal{G}_j\eta_j + \frac{4}{3}\sum_{j=5}^{7}\eta_j^*\mathcal{G}_j\eta_j + \text{c.c.}\Big)\psi + (\omega + B_2^\ell A^2)\frac{\psi^2}{2} + \frac{u}{4}\psi^4 + \frac{K}{2}|\vec{\nabla}\psi|^2\Big\}. \tag{B19}$$

Setting $\eta_j = \phi\exp(i\vec{q}_j\cdot\vec{r})$ as before gives

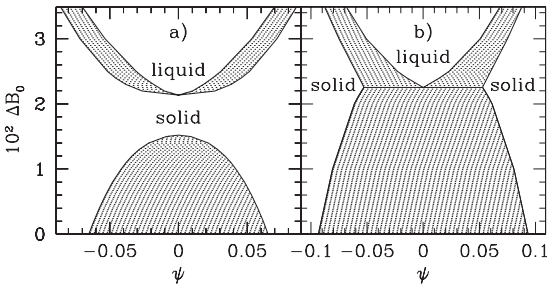

FIG. 8. Sample phase diagram for three-dimensional fcc system with the same parameter set and notation as in Fig. 1 except $\omega = 0.02$ in (a).

$$F = \int d\vec{r}\Bigg[\Bigg\{7\Delta B_0\phi^2 - 24t\phi^3 + \frac{693v}{2}\phi^4 + (\omega + 14B_2^\ell\phi^2)\frac{\psi^2}{2} + \frac{u}{4}\psi^4\Bigg\} - \Bigg\{\frac{K}{2}\psi\nabla^2\psi + 32B_0^x\left(\frac{1}{3} + \alpha\psi\right)\phi\nabla^2\phi\Bigg\} + \frac{16}{9}B_0^x\Bigg\{\sum_{i=1}^{3}\left(5U_{ii}^2 + 14\alpha\psi U_{ii} + \sum_{j\neq i}^{3}U_{ii}U_{jj}\right) + 4\sum_{i=4}^{6}U_{ii}^2\Bigg\}\phi^2\Bigg], \tag{B20}$$

from which the elastic constants for a fcc lattice can be obtained: $C_{11}=C_{22}=C_{33}=160B_0^x\phi^2/9$ and $C_{12}=C_{13}=C_{23}=C_{44}=C_{55}=C_{66}=32B_0^x\phi^2/9=C_{11}/5$.

Minimizing the above free-energy expression with respect to δ gives $\delta_{eq}=-\alpha\psi$ and hence the following free energy per unit volume:

$$\frac{F}{\mathcal{V}} = 7\Delta B_0\phi^2 - 24t\phi^3 + \frac{693}{2}v\phi^4 + (\omega + 7B_2^\ell\phi^2)\frac{\psi^2}{2} + \frac{u}{4}\psi^4 - \frac{112}{3}B_0^x(\alpha\phi\psi)^2, \tag{B21}$$

which is minimized when

$$\phi_{eq} = \frac{18t + \sqrt{324t^2 - 4851v[\Delta B_0 + \psi^2(B_2^\ell - 16B_0^x\alpha^2/3)]}}{693v}. \tag{B22}$$

A phase diagram for this fcc amplitude model is presented in Fig. 8.

[1] C. Harrison, D. H. Adamson, Z. D. Cheng, J. M. Sebastian, S. Sethuraman, D. A. Huse, R. A. Register, and P. M. Chaikin, Science **290**, 1558 (2000).
[2] V. Ginzburg and L. Landau, Zh. Eksp. Teor. Fiz. **20**, 1064 (1950).
[3] J. W. Cahn and J. E. Hilliard, J. Chem. Phys. **28**, 258 (1958).
[4] H. E. Cook, Acta Metall. **18**, 297 (1970).
[5] K. R. Elder, M. Katakowski, M. Haataja, and M. Grant, Phys. Rev. Lett. **88**, 245701 (2002).
[6] K. R. Elder and M. Grant, Phys. Rev. E **70**, 051605 (2004).
[7] J. Berry, K. R. Elder, and M. Grant, Phys. Rev. E **77**, 061506 (2008).
[8] J. Berry, M. Grant, and K. R. Elder, Phys. Rev. E **73**, 031609 (2006).
[9] J. Berry, K. R. Elder, and M. Grant, Phys. Rev. B **77**, 224114 (2008).
[10] J. Mellenthin, A. Karma, and M. Plapp, Phys. Rev. B **78**, 184110 (2008).
[11] Z.-F. Huang and K. R. Elder, Phys. Rev. Lett. **101**, 158701 (2008).
[12] Y.-M. Yu, R. Backofen, and A. Voigt (unpublished).
[13] C. V. Achim, M. Karttunen, K. R. Elder, E. Granato, T. Ala-Nissila, and S. C. Ying, Phys. Rev. E **74**, 021104 (2006).
[14] J. A. P. Ramos, E. Granato, C. V. Achim, S. C. Ying, K. R. Elder, and T. Ala-Nissila, Phys. Rev. E **78**, 031109 (2008).
[15] C. V. Achim, J. A. P. Ramos, M. Karttunen, K. R. Elder, E. Granato, T. Ala-Nissila, and S. C. Ying, Phys. Rev. E **79**, 011606 (2009).
[16] T. Hirouchi, T. Takaki, and Y. Tomita, Comput. Mater. Sci. **44**, 1192 (2009).
[17] P. Stefanovic, M. Haataja, and N. Provatas, Phys. Rev. E **80**, 046107 (2009).
[18] K. R. Elder, N. Provatas, J. Berry, P. Stefanovic, and M. Grant, Phys. Rev. B **75**, 064107 (2007).
[19] S. Majaniemi and M. Grant, Phys. Rev. B **75**, 054301 (2007).
[20] S. van Teeffelen, R. Backofen, A. Voigt, and H. Lowen, Phys. Rev. E **79**, 051404 (2009).
[21] A. Jaatinen, C. V. Achim, K. R. Elder, and T. Ala-Nissila, Phys. Rev. E **80**, 031602 (2009).
[22] R. Backofen, A. Ratz, and A. Voigt, Philos. Mag. Lett. **87**, 813 (2007).
[23] M. Cheng and J. A. Warren, J. Comput. Phys. **227**, 6241 (2008).
[24] S. M. Wise, C. Wang, and J. S. Lowengrub, SIAM (Soc. Ind. Appl. Math.) J. Numer. Anal. **47**, 2269 (2009).
[25] Z. Hu, S. M. Wise, C. Wang, and J. S. Lowengrub, J. Comput. Phys. **228**, 5323 (2009).
[26] G. Tegze, G. Bansel, G. Toth, T. Pusztai, Z. Fan, and L. Granasy, J. Comput. Phys. **228**, 1612 (2009).
[27] N. Goldenfeld, B. P. Athreya, and J. A. Dantzig, Phys. Rev. E **72**, 020601(R) (2005).
[28] B. P. Athreya, N. Goldenfeld, and J. A. Dantzig, Phys. Rev. E **74**, 011601 (2006).
[29] N. Goldenfeld, B. P. Athreya, and J. A. Dantzig, J. Stat. Phys. **125**, 1019 (2006).
[30] B. P. Athreya, N. Goldenfeld, J. A. Dantzig, M. Greenwood, and N. Provatas, Phys. Rev. E **76**, 056706 (2007).
[31] D.-H. Yeon, Z.-F. Huang, K. R. Elder, and K. Thornton, Philos. Mag. (to be published).
[32] K. A. Wu, A. Karma, J. J. Hoyt, and M. Asta, Phys. Rev. B **73**, 094101 (2006).
[33] K. A. Wu and A. Karma, Phys. Rev. B **76**, 184107 (2007).

[34] S. Majaniemi and N. Provatas, Phys. Rev. E **79**, 011607 (2009).
[35] N. Provatas and S. Majaniemi (unpublished).
[36] A. Karma and W.-J. Rappel, Phys. Rev. E **57**, 4323 (1998).
[37] K. R. Elder, M. Grant, N. Provatas, and J. M. Kosterlitz, Phys. Rev. E **64**, 021604 (2001).
[38] B. Echebarria, R. Folch, A. Karma, and M. Plapp, Phys. Rev. E **70**, 061604 (2004).
[39] T. V. Ramakrishnan and M. Yussouff, Phys. Rev. B **19**, 2775 (1979).
[40] S. W. Rick and A. D. J. Haymet, J. Chem. Phys. **90**, 1188 (1989).
[41] A. R. Denton and N. W. Ashcroft, Phys. Rev. A **42**, 7312 (1990).
[42] Z.-F. Huang, K. R. Elder, and N. Provatas (unpublished).
[43] M. C. Cross and P. C. Hohenberg, Rev. Mod. Phys. **65**, 851 (1993).
[44] G. H. Gunaratne, Q. Ouyang, and H. L. Swinney, Phys. Rev. E **50**, 2802 (1994).
[45] P. C. Hohenberg and B. I. Halperin, Rev. Mod. Phys. **49**, 435 (1977).
[46] K. R. Elder, F. Drolet, J. M. Kosterlitz, and M. Grant, Phys. Rev. Lett. **72**, 677 (1994).
[47] F. Drolet, K. R. Elder, M. Grant, and J. M. Kosterlitz, Phys. Rev. E **61**, 6705 (2000).
[48] L. Landau and E. Lifsitz, *Theory of Elasticity*, 3rd ed. (Butterworth-Heinemann, Oxford, 1999).
[49] E. Cadel, A. Fraczkiewicz, and D. Blavette, Annu. Rev. Mater. Res. **33**, 215 (2003).
[50] J. Wilde, A. Cerezo, and G. D. W. Smith, Scr. Mater. **43**, 39 (2000).
[51] A. H. Cottrell and B. A. Bilby, Proc. Phys. Soc., London, Sect. A **62**, 49 (1949).
[52] K. A. Jackson and J. D. Hunt, Trans. Metall. Soc. AIME **236**, 843 (1966).
[53] K. A. Jackson and J. D. Hunt, Trans. Metall. Soc. AIME **236**, 1129 (1966).
[54] S. Akamatsu and G. Faivre, Phys. Rev. E **61**, 3757 (2000).
[55] V. M. Orera, R. I. Merino, J. A. Pardo, A. Larrea, J. I. Pena, C. Gonzalez, P. Poza, J. Y. Pastor, and J. Llorca, Acta Mater. **48**, 4683 (2000).
[56] M. Haataja, J. Mahon, N. Provatas, and F. Léonard, Appl. Phys. Lett. **87**, 251901 (2005).
[57] M. Huang, C. S. Ritz, B. Novakovic, D. Yu, Y. Zhang, F. Flack, D. E. S. P. G. Evans, I. Knezevic, F. Liu, and M. G. Lagally, ACS Nano **3**, 721 (2009).
[58] H.-J. Kim-Lee, D. E. Savage, C. S. Ritz, M. G. Lagally, and K. T. Turner, Phys. Rev. Lett. **102**, 226103 (2009).
[59] K.-A. Wu, Ph.D. thesis, Northeastern University, 2006.
[60] J. A. Warren and W. J. Boettinger, Acta Metall. Mater. **43**, 689 (1995).
[61] W. J. Boettinger, J. A. Warren, C. Beckermann, and A. Karma, Annu. Rev. Mater. Res. **32**, 163 (2002).
[62] B. Nestler, H. Garcke, and B. Stinner, Phys. Rev. E **71**, 041609 (2005).